LAMINAR-TURBULENT TRANSITION CONTROL ON A SWEPT WING BY MICRON-SIZED ROUGHNESS ELEMENTS

D. Arnal, G. Casalis, E. Piot
(daniel.arnal@onecert.fr, gregoire.casalis@onecert.fr, estelle.piot@onecert.fr)
ONERA Centre de Toulouse
Département Modèles pour l'Aérodynamique et l'Energétique (DMAE)
2 avenue Edouard Belin – BP 4025 – 31055 Toulouse cedex

Summary
This paper describes a series of numerical investigations aimed at validating the concept of transition control by small roughness elements. Linear and nonlinear stability analyses are carried out in order to identify the most interesting pressure gradients and the Reynolds number range adapted for this type of control. Then the mechanisms leading to the formation of stationary vortices downstream of the roughness elements are investigated by Direct Numerical Simulations.

1. INTRODUCTION

Delaying the onset of laminar-turbulent transition on aircraft wings can reduce significantly the skin friction drag. Many theoretical, numerical and experimental investigations have demonstrated that “natural” transition is triggered by the breakdown of unstable waves generated by the disturbances which are present either in the free-stream (noise) or at the wall (surface defaults). On swept wings, distinction is made between Tollmien-Schlichting (TS) and crossflow (CF) waves. TS waves are the result of the instability of the boundary layer streamwise mean velocity profiles; they develop in regions of zero or positive pressure gradients. CF waves are the result of the instability of the boundary layer crossflow mean velocity profiles; they are unstable in regions of negative pressure gradient (accelerated flow), typically in the vicinity of the leading edge. A peculiar feature of CF instability is that zero frequency waves are highly amplified. They take the form of stationary vortices almost aligned with the external streamlines. Their initial amplitude is strongly linked with the wing surface polishing.

Three strategies are currently used in order to extend the laminar flow area: NLF (Natural Laminar Flow), LFC (Laminar Flow Control by suction at the wall) and HLFC (Hybrid Laminar Flow Control). These techniques have been widely used for many years and proved their efficiency.

Quite recently, an innovative solution for transition control has been proposed by W.S. Saric and his team at Arizona State University (ASU) [1], [2], [3], [4]. It applies to the transition process dominated by the stationary vortices resulting from a “pure” CF instability. These vortices have a wavelength λ_t which can be computed from the linear stability theory. The idea is to artificially create stationary vortices by using a spanwise row of micron-sized roughness elements (MSR) close to the leading edge. The wavelength λ_k of the new vortices corresponds to the spacing between the roughness elements. For particular values of λ_k and for particular pressure gradients, the nonlinear interactions between natural and artificial vortices result in a reduction of the amplitude of the natural vortices (target modes). From a physical point of view, the artificial vortices (killer modes) create a steady distortion of the mean flow, which leads to a strong decrease in the growth rate of the target vortices. At the same time, if the amplitude of the killer modes remains below some critical threshold, transition is delayed.

The general objective of this paper is to present a series of numerical investigations aimed at validating this new concept of transition control. The computations can be divided into two groups: one group dealing with stability analyses (linear and nonlinear), the second group dealing with Direct Numerical Simulations (DNS).

The computations based on stability analyses are described in paragraph 2. After a brief description of the linear and nonlinear stability codes used in this study, these numerical tools are applied to several existing swept wing models. The goal is to determine if particular combinations of the geometrical and aerodynamic parameters would be suitable for a successful application of the transition control by roughness elements.

The major shortcoming of the previous computations is that the roughness dimensions (in m) are ignored. They are represented in a more or less empirical way by imposing some initial velocity fluctuations (in ms^{-1}) in the nonlinear stability computations. This is why DNS computations have been undertaken. The results of these fundamental investigations are presented in section 3. The objective is to examine in detail the receptivity mechanisms, i.e. to understand how the disturbances generated by the small roughness elements are transformed into stationary vortices and, hopefully, to establish the link between the dimensions of the roughness elements and the initial amplitude of the killer vortices.

2. LINEAR AND NONLINEAR STABILITY ANALYSES

Numerical tools

Linear phase

The oldest method to characterise the boundary layer instabilities is based on the well-known linear Orr-Sommerfeld equation. The disturbances are written as:

$$r' = \hat{r}(y)\exp\left[i(\alpha x + \beta z - \omega t)\right]$$

r' is a velocity, pressure or density fluctuation. $\hat{r}$ is an amplitude function. *y* is normal to the surface. On a swept wing, *x* is measured along the wing surface in the direction normal to the leading edge, *z* is the spanwise direction. In the framework of the spatial theory, α and β are complex numbers representing the wave number components in the *x* and *z* directions; ω is real and represents the wave frequency. Assuming that the mean flow is parallel, the introduction of the previous expression into the linearised Navier-Stokes equations leads to ordinary differential equations for the amplitude functions. Numerically, one has to solve an eigenvalue problem: when the mean flow is specified, nontrivial solutions exist for particular combinations of (α, β, ω) only.

The linear PSE (Parabolized Stability Equations) approach provides an improvement to the Orr-Sommerfeld theory [5]. The mean flow field and the amplitude functions now depend on both *x* and *y*, and α depends on *x*. With the assumption that the *x*-dependence is slow, the numerical problem consists in solving a set of (nearly) parabolic equations in *x*, with initial disturbance profiles specified at some starting point x_0. The PSE make it possible to take into account the nonparallel effects as well as the wall curvature. However, the results are usually very close to those of the parallel theory.

To predict transition, the most popular method is the e^N criterion. The so-called *N* factor is the total growth rate of the most unstable disturbances. It is computed by integrating $-\alpha_i$ (opposite of the imaginary part of α) in the streamwise direction. It is assumed that transition occurs for some specified value N_t of *N*. N_t is usually close to 10 when CF disturbances play the major role in the transition process.

Nonlinear phase

The main interest of the linear PSE is to provide initial conditions for the nonlinear PSE which simulate the nonlinear wave interactions [5]. The disturbances are now expressed as a double series of (*n, m*) modes of the form:

$$r' = \sum_{n=-\infty}^{n=+\infty}\sum_{m=-\infty}^{m=+\infty} \hat{r}_{nm}(x,y)\exp\left[i\left(\int \alpha_{nm}(\xi)d\xi + m\beta z - n\omega t\right)\right]$$

α_{nm} is complex, β and ω are real numbers. The integers *n* and *m* characterise the frequency and the spanwise wavenumber, respectively. When these disturbances are introduced into the Navier-Stokes equations, a system of coupled partial differential equations is obtained; it is solved by a marching procedure, as it was already the case for the linear PSE. Any nonlinear PSE computation requires i) to choose the "most interesting" interaction scenario between particular modes which are referred to as major modes, ii) to impose initial amplitudes for the major modes. For two-dimensional flows, nonlinear computations end with a sudden increase of the major modes and of their harmonics; this simulates the appearance of turbulence. For three-dimensional flows governed by CF waves, the nonlinear interactions result in a saturation of the amplitude of all the modes, then the computation breaks down. It is generally assumed that transition starts "somewhere" between the beginning of the numerical saturation and the abscissa where the calculation ends. A more accurate transition prediction would require to use a secondary instability theory.

Successive steps of the computations

For a given configuration, the successive steps of the computations can be summarized as follows:

- The mean flow field is first determined from laminar boundary layer computations (3C3D code [6]).

- Then **linear, local** stability computations are performed with the CASTET code [7], [8] in order to determine the naturally most unstable wavelength λ_t (target mode). At this stage, the interaction scenario with the killer mode and the wavelength λ_k of this mode must be chosen.

- Then **linear, nonlocal** stability computations provide the disturbance initial profiles which are necessary for starting the nonlinear computations (FANNY code [9]).

- Finally **nonlinear** computations are carried out for given initial amplitudes of the natural and artificial stationary vortices (NELLY code [9]). This procedure is repeated with several initial amplitudes until an "interesting" interaction scenario is found. If no interesting scenario is identified, a new value of λ_k must be considered.

Parametric study for existing wings

After the numerical tools have been validated by comparison with the experimental data of Saric et al (see details in [10]), a parametric investigation was undertaken for several swept wing models available at ONERA. These models have been previously tested in wind tunnel in natural conditions, i.e. without control. Three airfoils have been selected:

- The ONERA D airfoil, tested in a research wind tunnel at ONERA Toulouse;

- The DTP A airfoil, tested in the F2 wind tunnel at ONERA Le Fauga-Mauzac;

- The DTP B model, also tested in the F2 wind tunnel.

The objective is to determine in which conditions (sweep angle, angle of attack, Reynolds number) these models could be used in the future for fundamental transition control experiments.

<u>An example of numerically successful transition control</u>

In order to illustrate in detail the successive numerical steps, a configuration related to the DTP B model has been chosen. A photograph of this model mounted on the floor of the F2 wind tunnel is shown in Figure 1. The chord C normal to the leading edge is 0.7 m, the relative thickness is 13,4% and the span is about 2.5 m. The results described below correspond to a sweep angle φ equal to 40°, an angle of attack α equal to -6° and a free stream velocity V_0 equal to 70 ms^{-1}. In these conditions, the chord Reynolds number Rc is close to 3.3 10^6.

Figure 1- The DTP B model in the F2 wind tunnel

The measured free-stream velocity distribution on the lower side (deduced from the measured pressure distribution) is plotted in Figure 2, where s is the distance normal to the leading edge, measured on the wing surface (it is thus the same distance as the one previously denoted as x). Experimentally, transition takes place at $s/C \approx 0.3$, i.e. in a region of strong negative pressure gradient. Therefore transition is expected to be triggered by a pure CF instability.

Using the free-stream velocity data of Figure 2, laminar boundary layer computations are carried out. They provide the necessary data for linear, local stability computations. As we are interested in stationary waves only, the computations are restricted to $\omega = 0$.

From these stability results can be determined the most amplified spanwise wavenumber $\beta_t = 2\pi/\lambda_t$ associated with the target mode (0,2) (see Table below). The corresponding N factor at transition is close to 10, a value which is classical for CF induced transition.

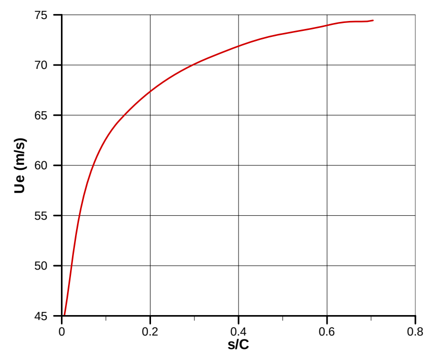

Figure 2- External velocity distribution

At this stage, the interaction scenario to be investigated by nonlinear PSE must be chosen. The most difficult problem lies in the choice of the killer mode. In the ASU experiments, MSR with a spanwise wavelength λ_k = 2/3 λ_t (or β_k = 3/2 β_t) resulted in a significant delay of the transition point. The same ratio was adopted in the present computations. Consequently, the following modes were accounted for in the nonlinear calculations:

mode	λ (mm)	Initial amplitude	Nature
(0,1)	2 λ_t	A_0	--
(0,2)	λ_t	A_1	target
(0,3)	2/3 λ_t	A_2	killer

The (0,1) mode is more or less a "numerical artefact". It represents the artificial first term of a series β^*, $2\beta^*$, $3\beta^*$, where $\beta_t = 2\beta^*$ and $\beta_k = 3\beta^*$ are the target and killer wave numbers linked together by β_t/β_k = 2/3.

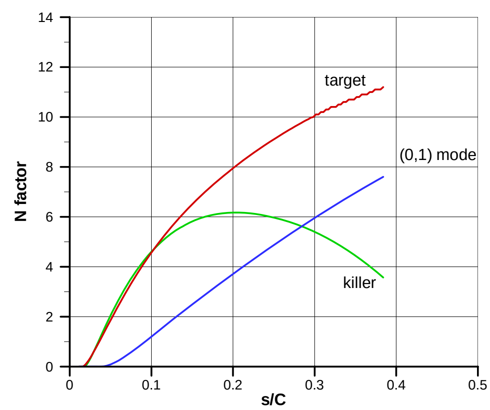

Figure 3- Linear, local N factors

Figure 3 shows the linear, local N factors for the (0,1), (0,2) and (0,3) modes. The corresponding linear, nonlocal evolutions are shown in Figure 4. Let us recall that the linear, nonlocal results are used as initial conditions for the nonlinear calculations. This means that they need to be determined at the initial x-station only. In the present example, however, nonlocal computations were continued up to the end of the computational domain in order to illustrate the influence of nonlocal (nonparallel) effects. It can be seen that the nonparallel effects are destabilizing: the nonlocal transition N factor is close to 12.

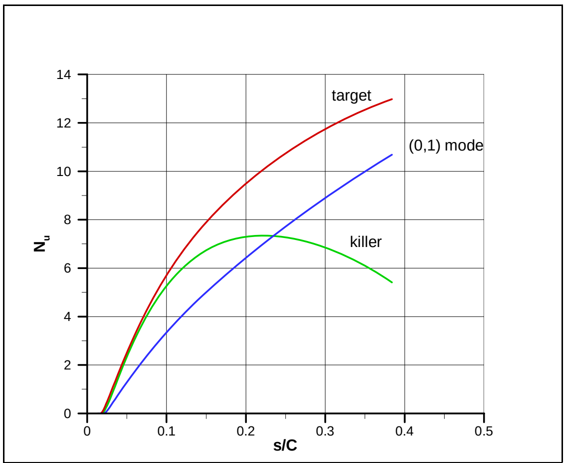

Figure 4- Linear, nonlocal N factors

Twelve modes, from (0,0) to (0,11) were considered in the nonlinear PSE computations. The (0,1), (0,2) and (0,3) modes are the major modes, for which some initial amplitude needs to be prescribed. The initial amplitude of the other modes is generated by the code. The (0,0) mode describes the spanwise independent distortion of the mean flow.

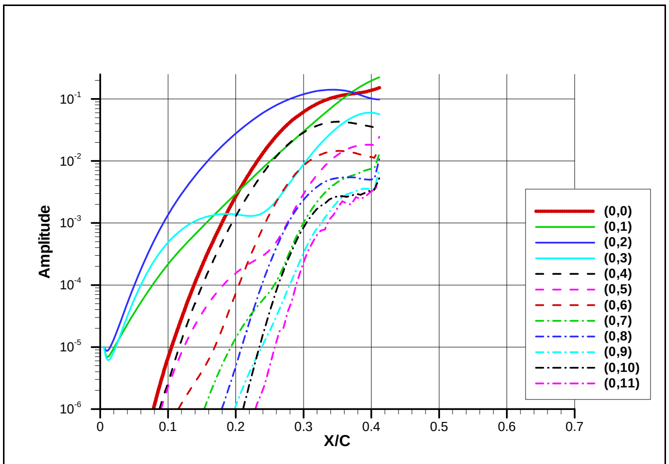

Figure 5- Nonlinear PSE results with $A_0 = A_1 = A_2 = 10^{-5}$, logarithmic scale

Figure 5 presents the chordwise evolution of the mode amplitude, with a vertical logarithmic scale. The results have been obtained with $A_0 = A_1 = A_2 = 10^{-5}$. As it is usually observed for pure CF transitions, a nonlinear saturation takes place between $x/C = 0.3$ and $x/C = 0.4$, just before the computation breaks down. As the experimental onset of transition is located at $x/C \approx 0.3$, this will be considered as the reference case without control.

In order to simulate the effects of roughness elements, the initial amplitude A_2 is now increased, A_0 and A_1 remaining constant. The results with $A_2 = 10^{-3}$ are plotted in Figure 6. The amplitude of the target decreases and the numerical breakdown occurs later than in the uncontrolled case. This can be considered as a case of numerically successful transition control.

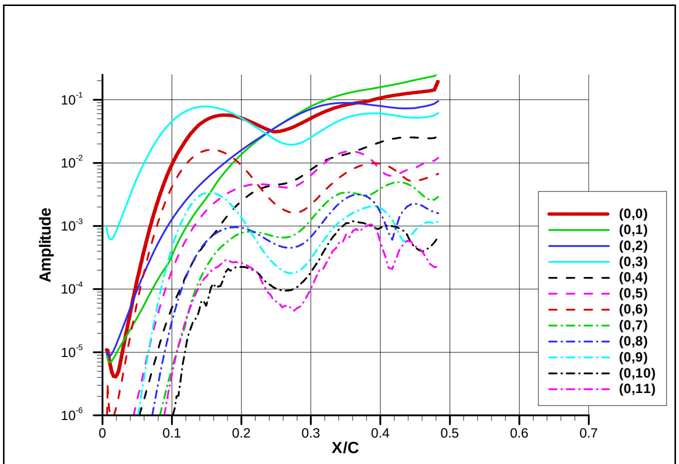

Figure 6- Nonlinear PSE results with $A_0 = A_1 = 10^{-5}$, $A_2 = 10^{-3}$, logarithmic scale

The amplitudes of the target and killer modes are plotted as a function of x/C with a linear scale for A_2 between 10^{-5} and 3 10^{-3}. The full lines (respectively the dotted lines) represent the target mode (respectively the killer mode). For a given computation, the same colour is used for both modes. The bold lines correspond to the reference case, i.e. $A_1 = A_2 = 10^{-5}$. When A_2 increases:

- the killer maximum amplitude increases;

- the target maximum amplitude decreases;

- for some values of A_2, the end of the computation moves downstream.

The conclusion is that the DTP B model in the conditions of the present computations could be a good candidate for an experimental validation of the concept of transition control by MSR.

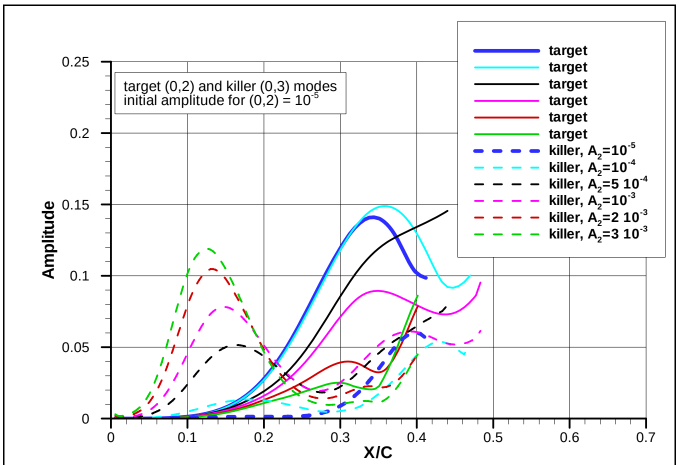

Figure 7- Evolution of the amplitude of the target and killer modes, linear scale

Systematic computations: typical results

As explained previously, systematic computations were carried out for three swept wings (ONERA D, DTP A, DTP B), see detailed results in [10]. From these calculations, practical rules for a successful (numerical) application of transition control by MSR were established. Two conditions related to the linear stability results need to be fulfilled:

- The "natural" transition must be triggered by zero frequency disturbances, with N factors for the "target" mode around 10 at the transition onset;
- The "killer" N factor must exhibit a maximum upstream of the "natural" transition location, with values around 6 according to the linear, local theory.

The curves plotted in Figure 3 clearly obey these rules. As a consequence, the corresponding nonlinear calculations led to positive results with appropriate initial amplitudes for the target and killer modes. However, the numerical examples discussed below show that the situation is not always so favourable.

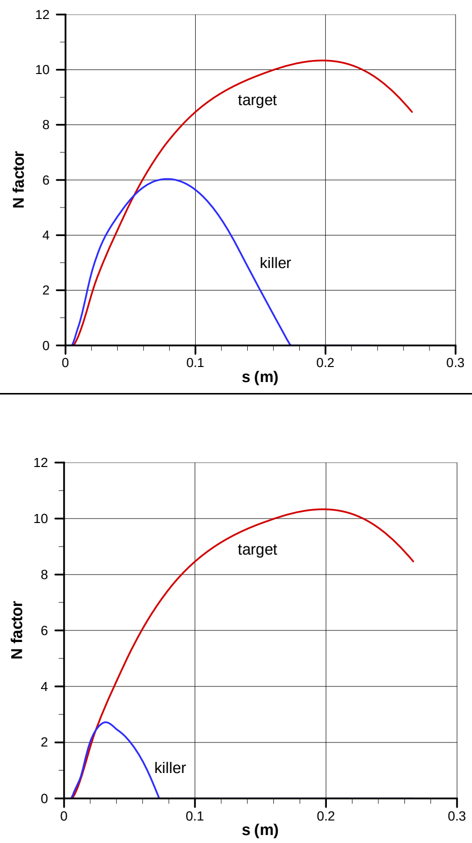

Figure 8- Two interactions scenarios for the ONERA D airfoil : λ_k/λ_t = 2/3 (upper) and λ_k/λ_t = 1/2 (lower)

The first example is related to the ONERA D airfoil. The sweep angle is 60°, the angle of attack -8°, and the chord Reynolds number Rc close to 3 10^6. The spanwise wavenumber β_t of the most amplified stationary vortices can be extracted at transition location ($s \approx 0.15$ m, or $s/C \approx 0.4$). It can be seen in Figure 8 that the transition N factor for the target mode is close to 10. The figure also shows the linear N factors for two interaction scenarios, one with λ_k/λ_t = 2/3, the other with λ_k/λ_t = 1/2. The nonlinear PSE results reveal that the first scenario is suitable for transition control by MSR. By contrast, with the second scenario, the maximum N factor for the killer mode is too low, so that no interesting result was obtained from the nonlinear PSE computations.

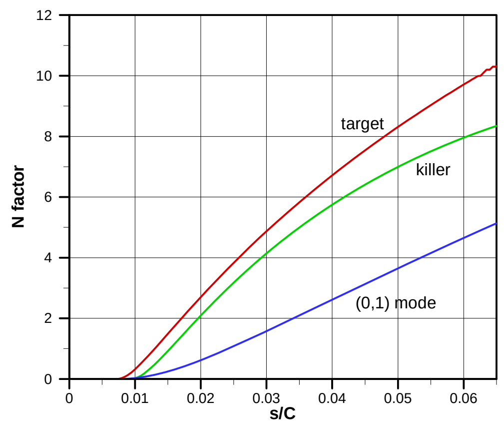

Figure 9- Results for the DTP B model at high Reynolds number

A common conclusion from the DTP B and ONERA D investigations is that the scenario λ_k/λ_t = 2/3 is powerful for this kind of control. Unfortunately, this is not a general rule, because the optimum ratio λ_k/λ_t depends on the Reynolds number. This is illustrated in Figure 9, which corresponds to the DTP B airfoil at a chord Reynolds number equal to 9 10^6, nearly 3 times the value considered in Figure 3. Here, transition is assumed to occur at $s/C \approx 0.06$, i.e. at the location where the target N factor is equal to 10. When the scenario λ_k/λ_t = 2/3 is adopted, the N factor curve for the killer mode is very different from that found for the low Reynolds number case, see Figure 3. This curve increases continuously from the critical abscissa to the transition location, and the PSE computations reveal that control is not possible: as soon as the initial amplitude of the killer mode is increased, the point where the computation breaks down moves upstream, indicating that the killer mode becomes responsible for the breakdown to turbulence.

These computations demonstrated that the wavelength of the killer vortices plays an important role in the control process. On the other side, the most interesting nonlinear results were obtained by assuming an initial amplitude of the killer modes of the order of 10^{-3}. The next problem is to estimate which roughness height corresponds to this initial value. Direct Numerical Simulations help to answer this question.

3. DIRECT NUMERICAL SIMULATIONS

In order to understand how the stationary vortices are generated downstream of the roughness elements, a Direct Numerical Simulation has been carried out. It aims at establishing the link between the initial amplitude of the killer vortices (in ms^{-1}) and the characteristic size of the surface imperfections (in m).

Configuration

The leading edge of a realistic swept wing is modelled as an infinite swept cylinder with a radius R_c. The cylinder is placed in a uniform and constant incoming flow with the velocity Q_∞ and the sweep angle φ. The associated unit Reynolds number is about 3.3 10^6 m^{-1}. The chordwise, wall-normal, spanwise directions are denoted as x, y, z, respectively. A spanwise periodic array of roughness elements is placed on the cylinder surface at the chordwise distance $x_r/R_c=8°$ from the attachment line, as shown in Figure 10. Thanks to the spanwise periodicity, only one roughness element is included within the computational domain. The spanwise center of the computational domain is fixed at the middle of the roughness element.

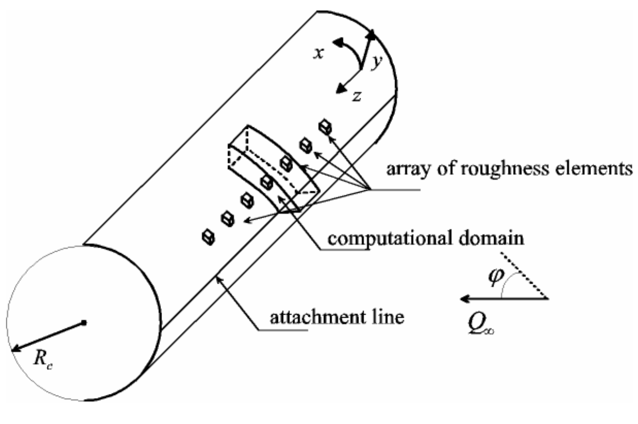

Figure 10- Sketch of the geometrical configuration.

The boundary layer along the cylinder is laminar and its thickness at the leading edge is denoted as δ. The roughness elements are parallelepipedic and their dimensions are denoted as (l_x, h, l_z) in the (x, y, z) directions, respectively. Four cases for the roughness size have been analysed, they are detailed in Table 1.

	Case 1	Case 2	Case 3	Case 4
l_x/δ	1.6	1.6	1.6	1.6
h/δ	0.1	0.075	0.05	0.1
l_z/δ	1.6	1.6	1.6	9.6

Table 1: List of the four considered cases. In the first three cases only the roughness element height is varied, while the fourth case corresponds to a roughness element with a large spanwise extent.

In each case the roughness height is small enough not to trigger the transition to turbulence, but is larger than the limit of linear receptivity, i.e. the roughness elements generate boundary layer disturbances that cannot be predicted by linear models. That is why a Direct Numerical Simulation of the Navier-Stokes equations is performed.

Numerical procedure

The compressible Navier-Stokes equations have been solved with the ONERA in-house solver sAbrinA, which is usually dedicated to aeroacoustics issues, see [11]. For the present computations, the compressibility effects are assumed to be negligible. The flow is modelled as an ideal gas with a specific heat ratio of 1.4, a Prandtl number of 0.72. The dynamic viscosity is computed thanks to Sutherland's law. The Navier-Stokes equations are discretized using high-order numerical schemes and structured multi-block meshes. The spatial scheme is a classical fourth-order accurate centered explicit finite difference discretization, while a compact explicit third-order accurate Runge-Kutta algorithm is used for time advancement. The grid is three-dimensional, structured and curvilinear. Eight subdomains are used and one of them corresponds to the roughness element location. For more details on the numerical method and boundary conditions, the reader is referred to [12].

The computation is performed in two successive steps. In the first one, the Navier-Stokes equations are solved on the "smooth" cylinder, i.e. without the roughness element. In that case the eighth sub-domain, which corresponds to the location of the roughness element itself, is part of the flow. The inviscid analytical flow field along the infinite-span cylinder is imposed as initial condition. After some transient a steady flow is obtained, which is called the ``base flow".
In the second step, the roughness element is present. Therefore the eighth domain is dropped and no-slip boundary conditions are imposed on its surface. The base flow is imposed as initial condition on each mesh point of the remaining seven sub-domains.
The specificity of this computation is thus that the roughness element is meshed and that no-slip boundary conditions are directly imposed at its walls. Moreover, the surface curvature is taken into account.

Analysis of the first case

In this section, the results of the computation performed for the first geometrical configuration (see Table 1) are detailed.

Laminar flow on the "smooth" swept cylinder

As explained previously, we have first to compute the flow around the swept cylinder when there is not any roughness element on its surface. An example of result is shown in Figure 11, which provides the pressure as function of the time at the location $x/R_c \approx 10°$, $z=0$ and $y=\delta$. As expected, after some transient, the obtained flow is independent of the spanwise coordinate and is steady. This last observation can be emphasized: even if the obtained laminar base flow is unstable with respect to crossflow instability, the DNS does not exhibit this instability in the case of the perfectly smooth cylinder.

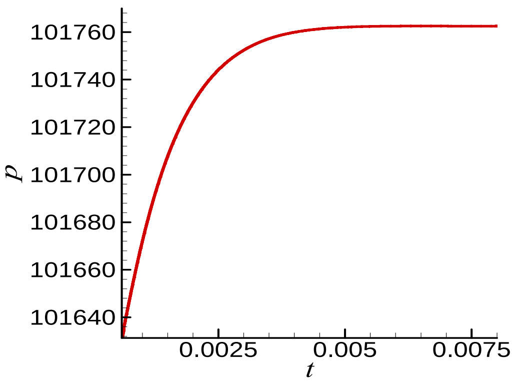

Figure 11-Pressure versus time on the "smooth" cylinder.

Flow perturbation induced by the roughness element

Next, the flow with a roughness element placed on the surface of the cylinder is computed. The computation starts from the base flow obtained in the smooth cylinder case. After a new transient, the signals extracted from locations downstream of the roughness element show that an unexpected unsteady perturbation takes place in the flow. This is illustrated by the pressure signal shown in Figure 12. This unsteady part is nearly harmonic with a frequency close to 3400 Hz.

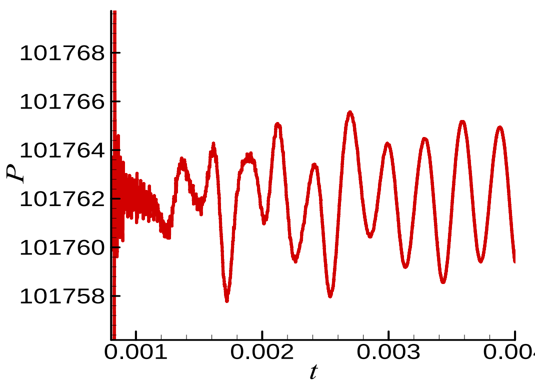

Figure 12-Pressure versus time in the presence of the roughness element.

It seems thus necessary to decompose the instantaneous flow field into a mean part and an unsteady one simply by performing an average value over a few periods. As the flow seems to be nearly harmonic this average procedure should not induce large numerical bias. The chordwise velocity component for instance is decomposed as:

$$u(x,y,z,t) = <u>_0 (x,y,z) + u^{unst}(x,y,z)\cos(\omega t + \Phi)$$

where $\omega/2\pi$ corresponds to the frequency (close to 3400 Hz) and Φ stands for a phase. Figure 13 displays the unsteady part of the chordwise velocity component as function of x and z at a constant distance from the wall ($y \approx 3.5h$, where h is the roughness element height. This corresponds to about one third of the boundary layer thickness). A careful analysis of the flow field shows that the unsteady waves are sinusoidal in the spanwise direction with a $2\beta_z$ spanwise wavenumber, where $\beta_z = 2\pi/\lambda_z$ is the wavenumber associated to the spanwise extent of the computational domain λ_z. Moreover, a comparison of their wall-normal evolution with the eigenfunctions obtained by an Orr-Sommerfeld analysis proves that the unsteady waves captured by the DNS are unsteady crossflow waves of frequency 3400 Hz and of spanwise wavenumber $2\beta_z$ [12]. Unfortunately, the amplitude of these waves is rather large: a few percents of the external velocity. Consequently, non-linear interaction occur between the unsteady flow field and the steady flow field.

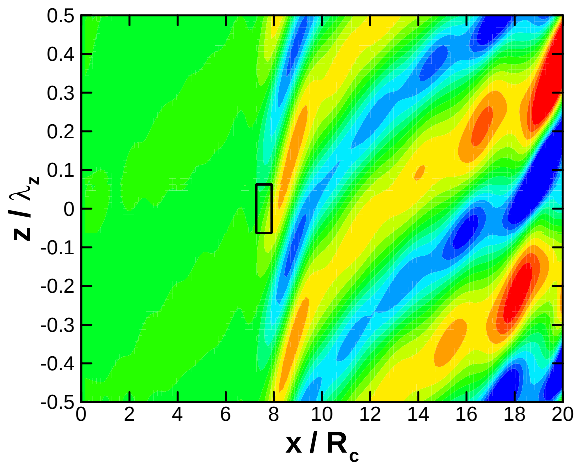

Figure 13- Iso-values of the unsteady chordwise velocity component at $y \approx 3.5h$. The roughness element location is plotted in black solid lines.

The steady flow field is plotted in Figure 14. The base flow has been subtracted from the total steady field to make the visualization of the steady perturbation induced by the roughness element possible. A strong flow deformation can be seen around the roughness location. Further downstream, steady oscillations associated to the β_z spanwise wavenumber appear. The DNS thus confirms that an array of roughness elements can generate stationary vortices, which had been previously observed in many experiments, see [1] for instance.

The stationary vortices are amplifying in the chordwise direction, with a growth rate that is much more important than the one predicted by the linear stability theory (Orr-Sommerfeld theory). This disagreement is due to the non-linearity created by the unsteady flow field, which consequently drives the steady flow amplification. Therefore, the initial amplitude of the stationary waves, which can be extracted from the DNS results, may not be intrinsic, and its quantitative value must be considered as a rough estimate only.

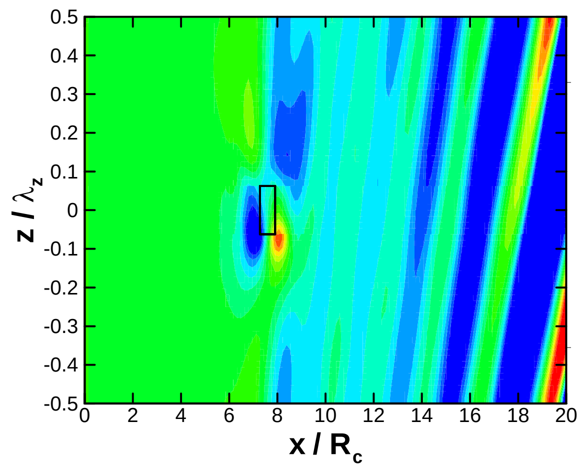

Figure 14- Iso-values of the steady chordwise velocity component at y ≈ 3.5h. The roughness element location is plotted in black solid lines.

Influence of the roughness size

The numerical procedure detailed in the previous section for the first case of roughness geometry is repeated for the three other cases presented in Table 1. It is important to notice that the base flow (i.e the flow around the smooth cylinder) is the same for each case. Only the roughness size differs from one case to another, and thus the strength of the crossflow waves excitation. The steady flow field is plotted for each case in Figures 15 (a-d). As in Figure 14, the base flow has been subtracted from the total steady flow. It must also be pointed out that the velocity scale is different from one figure to another.

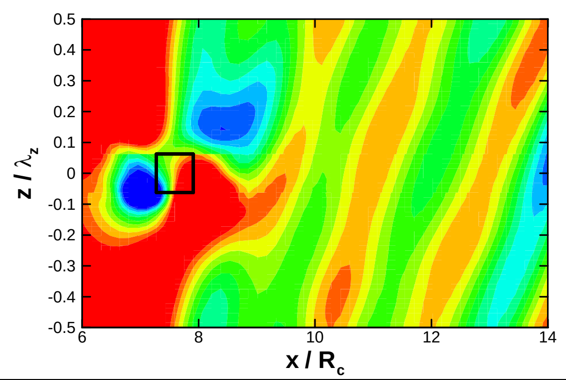

Figure 15 (a). Steady chordwise velocity in case 1

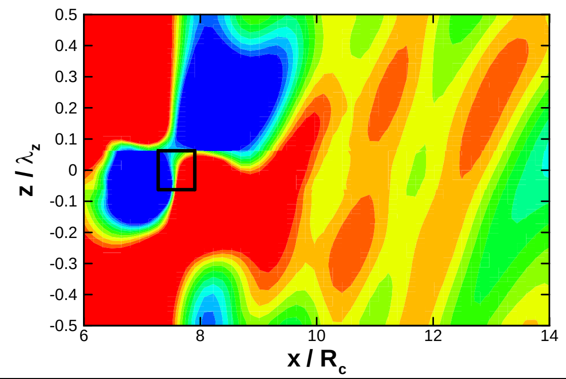

Figure 15 (b). Steady chordwise velocity in case 2

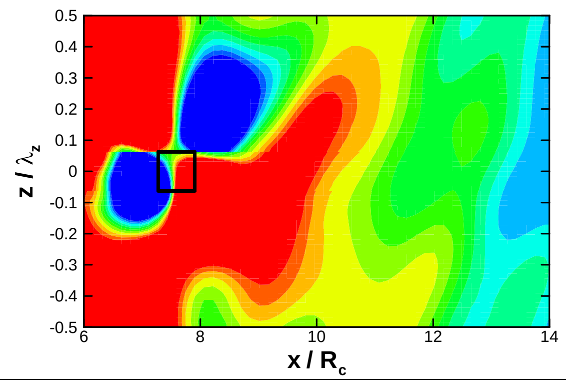

Figure 15 (c). Steady chordwise velocity in case 3

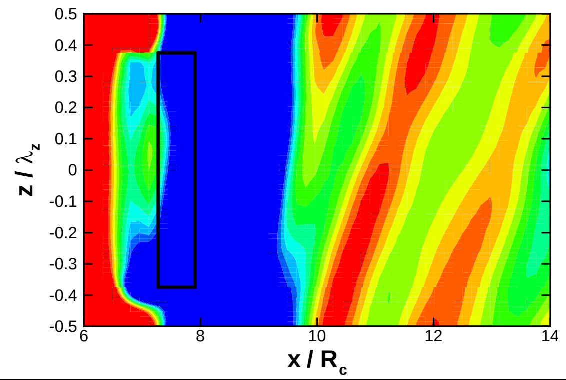

Figure 15 (d) . Steady chordwise velocity in case 4

A strong flow deformation can be seen around the roughness location, with different features between the first three cases and the fourth one. Further downstream stationary vortices can be observed. The amplitude of the velocity fluctuations induced by the vortices is similar for cases 1, 2 and 4, whilst it is significantly smaller for the third case. The initial amplitude of the stationary vortices seems to be driven by the features of the flow distortion in the roughness element vicinity. As explained previously, the presence of the unwanted unsteady crossflow waves influences significantly the steady flow field, and thus the initial amplitude of the stationary vortices. Consequently, an accurate receptivity investigation is impossible for the studied configuration. Anyway, the results show that the obtained initial amplitude is close to 10^{-3} of the external velocity. Even if this value must be considered in a qualitative way only for the present study, it shows that the values chosen for initializing the amplitude of the killer vortices in the nonlinear PSE computations (A_2) is in the correct range.

Further computations are currently undertaken in E. Piot's thesis [13] to get rid of the unsteady crossflow wave and consequently to be able to perform a more accurate receptivity investigation.

4. CONCLUSIONS

The linear and nonlinear stability computations have demonstrated that two conditions need to be fulfilled for a successful application of the control system by MSR:

- The uncontrolled transition N factor for stationary vortices must be large enough (around 10) in order to be sure that these vortices dominate the transition process.

- The N factor curves for the killer mode must exhibit a maximum upstream of the natural transition location, with a value around 6.

When these conditions are fulfilled, nonlinear PSE computations show that increasing the initial amplitude of the killer mode can delay the appearance of the numerical transition; in other words, the beginning of the nonlinear saturation and the point where the computation breaks down move downstream. Another important result is that there are no "good" and "bad" pressure gradients: a given pressure gradient can be convenient or not, depending on the Reynolds number.

The determination of the roughness height remains a key issue. The DNS results reported in section 3 brought many original information concerning the "birth" of CF vortices in the immediate vicinity of a roughness array. It has been found that a roughness element of height h equal to 5 or 10% of the boundary layer thickness generates vortices with an initial amplitude around 10^{-3} U_e. This is the order of magnitude of the most appropriate values of A_2 determined from the nonlinear analyses. However, the unexpected appearance of travelling waves hides a part of the receptivity process and provokes premature nonlinear interactions which make the DNS results difficult to interpret.

From the previous remarks, it is recommended to conduct future investigations in two ways:

- An experimental study is required in order to validate or invalidate the nonlinear PSE results. The effects of the shape and size of the roughness elements also need to be investigated and compared with the DNS data. The DTP B model could be convenient for these investigations.

- Further DNS studies are also necessary in order to clarify the origin of the (parasitic?) travelling waves. If it can be demonstrated that these waves result from a numerical artefact and if it is possible to reduce them, then the stationary vortices will exhibit a linear growth downstream of the critical point. This will enable to establish a more precise correspondence between h and A_2. This work is currently a part of E. Piot's thesis [27].

Acknowledgments

Part of the work described in the paper was carried out with the financial support of Airbus. The assistance of Marc Terracol in the use of the DNS code is gratefully acknowledged.

References

[1] R.H. Radetztsky Jr., M.S. Reibert, W.S. Saric, S. Takagi: Effect of micron-sized roughness in swept-wing flows, AIAA Paper 93-0076, 1993

[2] W.S. Saric, R.C. Carrillo, M.S. Reibert: Leading edge roughness as a transition control mechanism, AIAA Paper 98-0781, 1998

[3] W.S. Saric, H.L. Reed: Supersonic laminar flow control on swept wings using distributed roughness, AIAA Paper 2002-0147, 2002

[4] W.S. Saric, H.L. Reed: Crossflow instabilities. Theory and technology, AIAA Paper 2003-0771, 2003

[5] T. Herbert: Parabolized Stability Equations, in AGARD Report N° 793, 1993

[6] R. Houdeville, P. Malecki : Calculs de couches limites tridimensionnelles. Description et mode d'emploi du code 3C3D, RT ONERA/DERAT N° 65/5625.60-01, 1996

[7] D. Arnal: Etablissement et résolution des équations de stabilité en écoulement compressible. Exemple de résultats. RT ONERA/DERAT N° 35/5018, 1986

[8] J. Perraud : Calculs de stabilité linéaire de couches limites compressibles. Description et mode d'emploi du code CASTET. RT ONERA/DERAT N° 124/5118.32, 1997

[9] H. Salinas: Stabilité linéaire et faiblement non linéaire d'une couche limite laminaire compressible tridimensionnelle par l'approche PSE, Thesis, Supaero, June 1998

[10] D. Arnal, E. Piot, J.P. Archambaud, G. Casalis, C. Content, J. Dandois, S. Colamartino : TRACMIR : TRAnsition Control by Micron-sized Roughness elements, RF 2/12136 DMAE, November 2007

[11] M. Terracol. Développement d'un solveur pour l'aéroacoustique numérique : sAbrinA.

Tech. Report RT 5/07383 DSNA, ONERA, 2003.

[12] E. Piot, G. Casalis and M. Terracol. Direct Numerical Simulation of the crossflow instabilities induced by a periodic roughness array on a swept cylinder : receptivity and stability investigations. AIAA 2007-3976, 37th Fluid Dynamics Conference, Miami FL, June 25-28, 2007.

[13] E. Piot: Thesis, in preparation.